Warming from cold pools

A pathway for mesoscale organization to alter Earth's radiation budget

Alinaghi, Pouriya; Janssens, Martin; Jansson, Fredrik

DOI
10.1073/pnas.2513699122

Publication date
2025

Document Version
Final published version

Published in
Proceedings of the National Academy of Sciences of the United States of America

Citation (APA)
Alinaghi, P., Janssens, M., & Jansson, F. (2025). Warming from cold pools: A pathway for mesoscale organization to alter Earth's radiation budget. *Proceedings of the National Academy of Sciences of the United States of America*, *122*(49), Article e2513699122. https://doi.org/10.1073/pnas.2513699122

PNAS RESEARCH ARTICLE | EARTH, ATMOSPHERIC, AND PLANETARY SCIENCES

Warming from cold pools: A pathway for mesoscale organization to alter Earth's radiation budget

Pouriya Alinaghi[a,1,2,3], Martin Janssens[a,b,2,3], and Fredrik Jansson[a]

Affiliations are included on p. 9.

Edited by Isaac Held, Atmospheric and Oceanic Sciences Program, Princeton University, Princeton, NJ; received June 3, 2025; accepted October 23, 2025

Marine shallow cumulus clouds have long caused large uncertainty in climate projections. Such "trade cumuli" frequently organize into mesoscale (10 to 500 km) structures, through two processes that couple the clouds to shallow mesoscale circulations: i) mesoscale moisture aggregation and ii) cold pools, driven by mesoscale rain evaporation beneath the mesoscale cloud structures. Since global climate models do not capture these mesoscale processes, while the degree of mesoscale organization is observed to correlate to shortwave cooling, it has been suggested that mesoscale processes modulate contemporary estimates of cloud response to global warming. Here, we show that introducing mesoscale dynamics can indeed substantially alter top-of-the-atmosphere radiative budget, if the balance between the two circulations is upset. By homogenizing mesoscale rain evaporation patterns, we suppress the formation and effects of cold pools in a large ensemble of large-domain, large-eddy simulations. The experiments reveal that cold pool dynamics reduce mesoscale ascent in the cloud systems, thereby arresting a runaway self-aggregation of moisture into very moist, cloudy regions that occurs without them. This reduces the net rainfall of the cumulus fields, moistens the cloud layer and thus reduces the emission of clear-sky longwave radiation to space, giving an ensemble-averaged warming of 1.88 W/m^2. Our results highlight that the proper interplay between mesoscale processes is critical for capturing radiative budgets-especially in kilometer-scale climate models that only partially resolve shallow cumulus aggregation and cold pools.

mesoscale organization | shallow cumulus clouds | cloud feedbacks | rain evaporation | cold pools

Significance

Shallow cumulus clouds play a central role in Earth's energy balance, but remain a major source of uncertainty in climate projections. While climate models often assume these clouds are fully controlled by large-scale factors, observations show they organize into mesoscale patterns that strongly affect how much sunlight is reflected to space. The relevance to the cloud-climate feedback of the mesoscale processes which shape this organization is unknown. By homogenizing the evaporation of rain in large-domain, high-resolution simulations that resolve the cumulus clouds, we show that the interplay between mesoscale processes is key for radiative budgets. This suggests that under-resolving these processes in models can lead to substantial biases.

Uncertainties in the response of tropical shallow cumulus clouds to global warming are a long-standing source of uncertainty in climate projections (1–8). Such uncertainty is usually framed in terms of predictions of the "shortwave cloud feedback," the change in sunlight reflected back to space by clouds per unit warming of the tropical environment. Predictions of this feedback diverge among global climate models (GCMs) (1–3, 5), high-resolution atmospheric models (9, 10) and observation-based techniques (11, 12), because the models inadequately represent several cloud processes which are thought to control shortwave cooling (13–16).

One missing process class comprises "mesoscale processes." These act on horizontal scales of tens to hundreds of kilometers, and ubiquitously organize fields of shallow cumuli into mesoscale patterns (17–23). GCMs discretize the atmosphere too coarsely to resolve these processes, while detailed process models have traditionally covered domains too small for the cumuli to organize. Yet, mesoscale processes are hypothesized to influence the cloud feedback, because the cloud cover, cloud albedo, and in turn shortwave cooling of cumulus fields rise in proportion with their degree of mesoscale organization (21, 24, 25). However, it is not established whether such shortwave cooling changes with the degree of organization are actually caused by overlooked mesoscale processes, or if one can still correctly represent how cloud cover and cloud albedo respond to variations in the large-scale climatology, even without accounting for the mesoscale (6, 17). It is also not established whether mesoscale processes additionally affect the longwave component of the top-of-atmosphere (TOA) radiation budget, as is the case when deep cumulus clouds organize (26–29). Taken together, these points emphasize that to alter contemporary estimates of climate feedback, we require evidence that including mesoscale processes meaningfully alters the full TOA radiation budget of shallow cumulus regimes, given the same climatological forcing.

Here, we test this condition through detailed atmospheric process models, large-eddy simulations (LES) (30), on domains large enough to simulate mesoscale organization ($153.6 \times 153.6\,\mathrm{km}^2$). Under fixed and spatially homogeneous large-scale conditions,

The authors declare no competing interest.

This article is a PNAS Direct Submission.

[1]Present address: Department of R&D Weather and Climate Models, Royal Netherlands Meteorological Institute (KNMI) 3730AE, De Bilt, The Netherlands.

[2]P.A. and M.J. contributed equally to this work.

[3]To whom correspondence may be addressed. Email: p.alinaghi@tudelft.nl, pouriya.alinaghi@knmi.nl, or martin.janssens@wur.nl.

This article contains supporting information online at https://www.pnas.org/lookup/suppl/doi:10.1073/pnas.2513699122/-/DCSupplemental.

Published December 1, 2025.

these LESs produce mesoscale organization through two pathways: First, nonprecipitating cumulus clouds spontaneously self-aggregate into mesoscale clusters via shallow, self-reinforcing mesoscale circulations driven by condensational heating in the clouds (31–34). Second, as the cumuli deepen and begin to precipitate, rain evaporation in the cloudy columns forms pockets of cold, dense air. While downdrafts within these "cold pools" suppress cloud formation locally, their expanding fronts carry moist air and strong updrafts that trigger new cumuli, forming ring-like mesoscale cloud structures (35–45). In both pathways, water vapor and shallow cumulus clouds organize through mesoscale circulations, a coupling also recently observed in nature (13, 46–48). Yet, the two circulations are formed by distinct mesoscale processes: moisture self-aggregation and rain evaporation.

Previous work indicated that when both pathways are active in large-domain LESs, they always organize the clouds into mesoscale patterns. However, this organization does not appear to significantly affect the TOA radiative budgets, relative to small-domain simulations where neither process can act (49).

However, here we show that this result emerged from a balance of the two mesoscale processes, each of which individually can affect the climatological cooling of fields of shallow cumuli. To demonstrate this, we compare two otherwise identical, large-domain LES ensembles: CP, where both mesoscale processes operate normally, and NoCP, where we inhibit the local effects of rain evaporation. Specifically, instead of allowing rain evaporation to locally cool the atmosphere and make it negatively buoyant, we redistribute this cooling evenly across a horizontal model level, such that no negative buoyancy perturbations are created (50). This leaves the immediate domain-averaged drying and heating tendencies intact, but prevents the formation of cold pools, hence the name NoCP. It therefore also prevents all the subsequent effects that these cold pools would have had on mesoscale circulations, cloud organization, the horizontal and vertical distribution of water vapor, and ultimately on TOA radiation. Hence, we stress that the NoCP ensemble is designed to not just eliminate the presence of cold pools, but to capture *all* effects arising from removing rain evaporation variability at mesoscales.

Each ensemble consists of 19 LESs, which cover a range of marine shallow cumulus regime environments that are representative for today's climatology. These environments are characterized by "cloud controlling factors" (CCFs) (51–54), large-scale environmental parameters known to regulate cloud responses to warming in GCMs (55–57). Specifically, we vary the near-surface geostrophic wind speed $|u_0|$, subsidence w_1, stability Γ, and vertical wind shear u_z, over ranges derived from the ERA5 climatology (58, 59) (*Materials and Methods* and Table 1). These CCFs shape both the large-scale forcings and the initial conditions of the simulations. They were chosen because they are particularly relevant for cold pools: By varying them, cold-pool size and frequency span a range from nearly absent to frequent and large (44, 45). Because they control the range of cold pool variability, they also cover the range of potential impacts of rain evaporation homogenization on the radiation balance (*Materials and Methods*). Here, we use this setup for two assessments: First, by contrasting the two ensembles, we quantify the impact of mesoscale rain evaporation on the TOA radiation balance across a range of CCFs representative of Earth's trade-wind environments. And second, we compare the impact of rain evaporation homogenization to the variability in TOA radiation induced by varying the CCFs themselves, to judge its significance relative to sensitivities that are well-appreciated.

Both CP and NoCP ensembles are run for five daily cycles of insolation, starting from identical, cloud-free initial conditions. Initially, both evolve similarly as nonprecipitating cumuli self-aggregate via shallow circulations (Fig. 1 *A*–*C*). As clouds deepen and precipitation begins, cold pools emerge in the CP ensemble, forming mesoscale ring-like cloud structures enclosing clear-sky areas and suppressing the height of the near-surface well-mixed layer h_{mix} (Fig. 1*B*), consistent with prior modeling and observational studies (60, 61). In contrast, the NoCP ensemble precipitates without forming cold pools; h_{mix} remains elevated, and the clouds continue to self-aggregate without generating open-sky regions (Fig. 1*C*).

We trace the impact of cold pools on the TOA radiation budget in three parts. First, we quantify the difference in net TOA radiation between the CP and NoCP ensembles. We show that when cold pools are allowed to form and develop normally, they provide a significant warming at the TOA, relative to the simulations without cold pools. This results not from modifications in the fraction of reflected sunlight, but from reductions in the outgoing longwave clear-sky radiation. The reduced longwave cooling originates in the CP ensemble's more humid cloud layers. Thus, in the second part, we show that cold pools keep the cloud layer humid by producing less rainfall. Third, we demonstrate that cold pools reduce the surface rainfall, because they counteract the circulations which aggregate water vapor into very moist regions in their absence, thus preventing efficient rainfall in these regions. Hence, we suggest the key to understanding whether mesoscale processes alter the cloud feedback, lies in understanding the interplay between shallow mesoscale circulations and the field of low-lying water vapor.

Results

Cold Pools Warm by Reducing Clear-Sky Outgoing Longwave Radiation. The net TOA radiative budget N is expressed as $N = C_s + C_l - F^{\uparrow}_{s,c} - F^{\uparrow}_{l,c}$, where C_s and C_l represent the shortwave and longwave cloud-radiative effects, respectively, while $F^{\uparrow}_{s,c}$ and $F^{\uparrow}_{l,c}$ are the outgoing shortwave and longwave clear-sky fluxes. A positive contribution to N indicates energy accumulation and warming. All terms are domain- and time-averaged on day five for each CP and NoCP ensemble member, when the simulated cloud layers no longer change much. The mean TOA net radiation N for the CP ensemble exceeds that of the NoCP ensemble by 1.88 W/m^2 (Fig. 2*A*). The relative warming of the CP ensemble ($N_{\mathrm{CP}} - N_{\mathrm{NoCP}} > 0$) is consistent across 18 out of 19 ensemble members. This warming is mainly due to reduced $-F^{\uparrow}_{l,c}$ in the CP ensemble, as differences in C_s, C_l, and $F^{\uparrow}_{s,c}$ are negligible.

The muted response of C_s to homogenizing rain evaporation is composed of offsetting effects (Fig. 2*B*): reduced cooling from smaller cloud fraction ($F^{\downarrow}_s \alpha_c \Delta f$) is balanced by enhanced cooling from higher albedo in the CP ensemble ($F^{\downarrow}_s f \Delta\alpha_c$), where $F^{\downarrow}_s$ is the insolation flux (see *Materials and Methods* for cloud fraction f and cloud albedo α_c calculations). A 1.5 W/m^2 spread around ΔC_s arises from the CP ensemble's higher albedo and lower coverage, with their relative impact differing across the ensemble (adding more ensemble members with diverse CCFs would yield a more representative estimate of cold-pool impacts on C_s; see *Materials and Methods*). A similar compensation explains the minimal difference in C_l: Cloud fields in the CP ensemble feature smaller cloud fraction f, but contain deeper clouds. Both more and deeper clouds enhance longwave warming, and these effects offset.

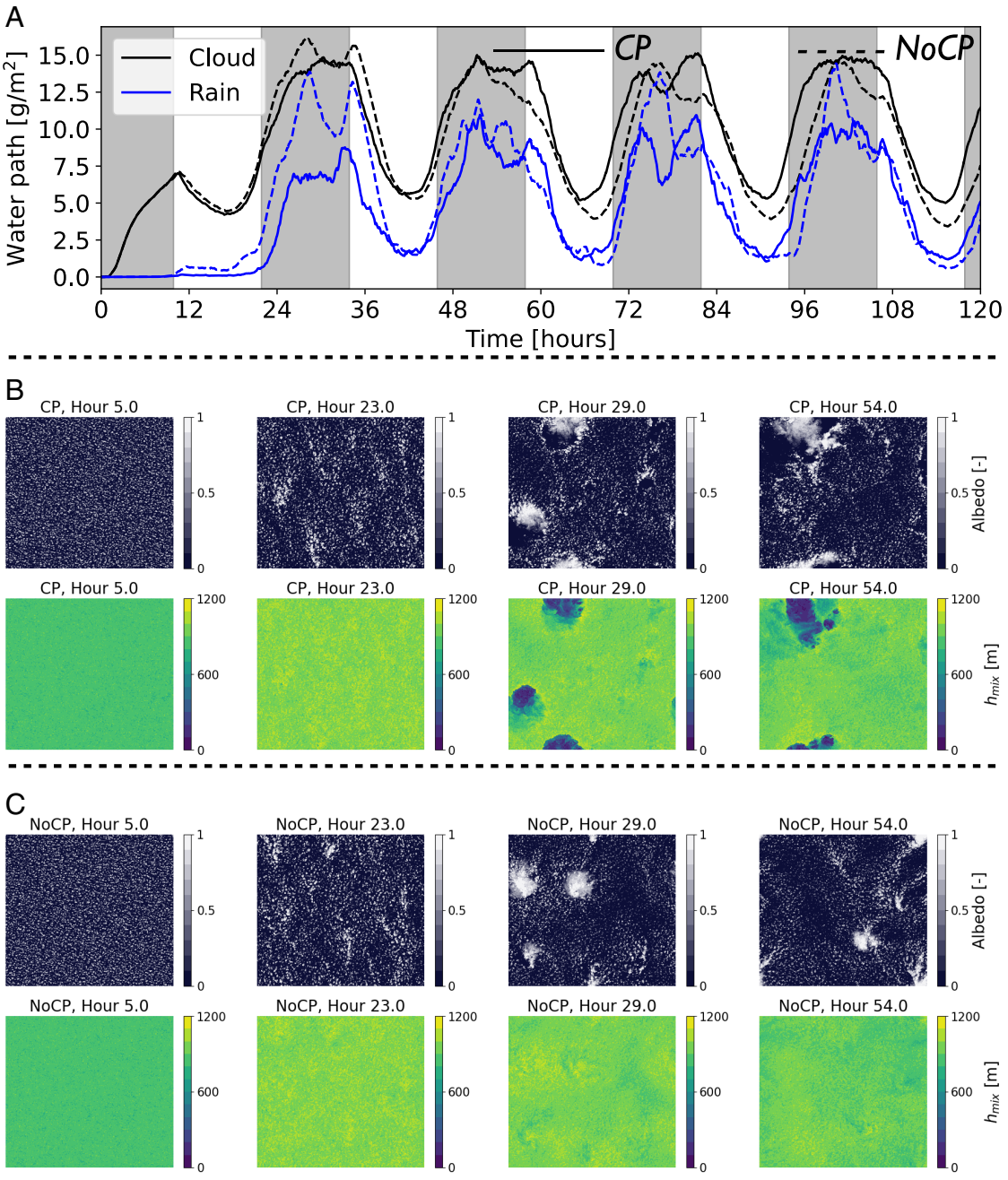

Fig. 1. Temporal evolution of cloud fields in both the CP and NoCP ensembles. (*A*) Time series of cloud- and rain-water paths averaged across the entire CP (continuous) and NoCP (dashed) ensembles. Gray shades show nighttime. (*B* and *C*) are the top-view fields of cloud albedo (first row) and mixed-layer height (second row) for the central reference simulation of the CP and NoCP ensembles, respectively.

Thus, the net warming from cold pools stems from $-\Delta F_{l,c}^{\uparrow}$. This can be attributed to the difference in the horizontally and temporally averaged vertically integrated total water mass (cloud + vapor) I between these CP and NoCP ensembles, $\Delta F_{l,c}^{\uparrow} \approx \partial_I F_{l,c}^{\uparrow} \Delta I$ (Fig. 2*C*). As the simulations evolve beyond the nonprecipitating phase (0 to 12 h), the CP ensemble-averaged I rises, while the NoCP simulations dry (Fig. 2*D*). The CP ensemble's warming from a less negative $-F_{l,c}^{\uparrow}$ follows this evolution, until it stabilizes on the fifth simulation day. On this day, the vertical distribution of horizontally averaged total-water specific humidity q_t (cloud water q_l + water vapor q_v in Fig. 2 *E* and *F*) reveals that the CP ensemble is primarily moister in the upper cloud layer, between 1,500 to 3,000 m. When capped by the dry overlying troposphere of the trades, adding water vapor to the cloud layer is known to effectively prevent the water vapor in the moister, underlying boundary layer from cooling to space (62). Indeed, the CP ensemble's upward longwave flux reduces in magnitude across this layer, and the resultant longwave cooling difference persists until TOA (Fig. 2 *E* and *F*).

The cold-pool-induced warming is significant: Multivariate regression of $-F_{l,c}^{\uparrow}$ onto the CCFs shows that cold pools have a greater impact on $-F_{l,c}^{\uparrow}$ compared with a unit of change in $|u_0|$, w_1, or u_z (Fig. 2*H*). Only enhancing the free-tropospheric

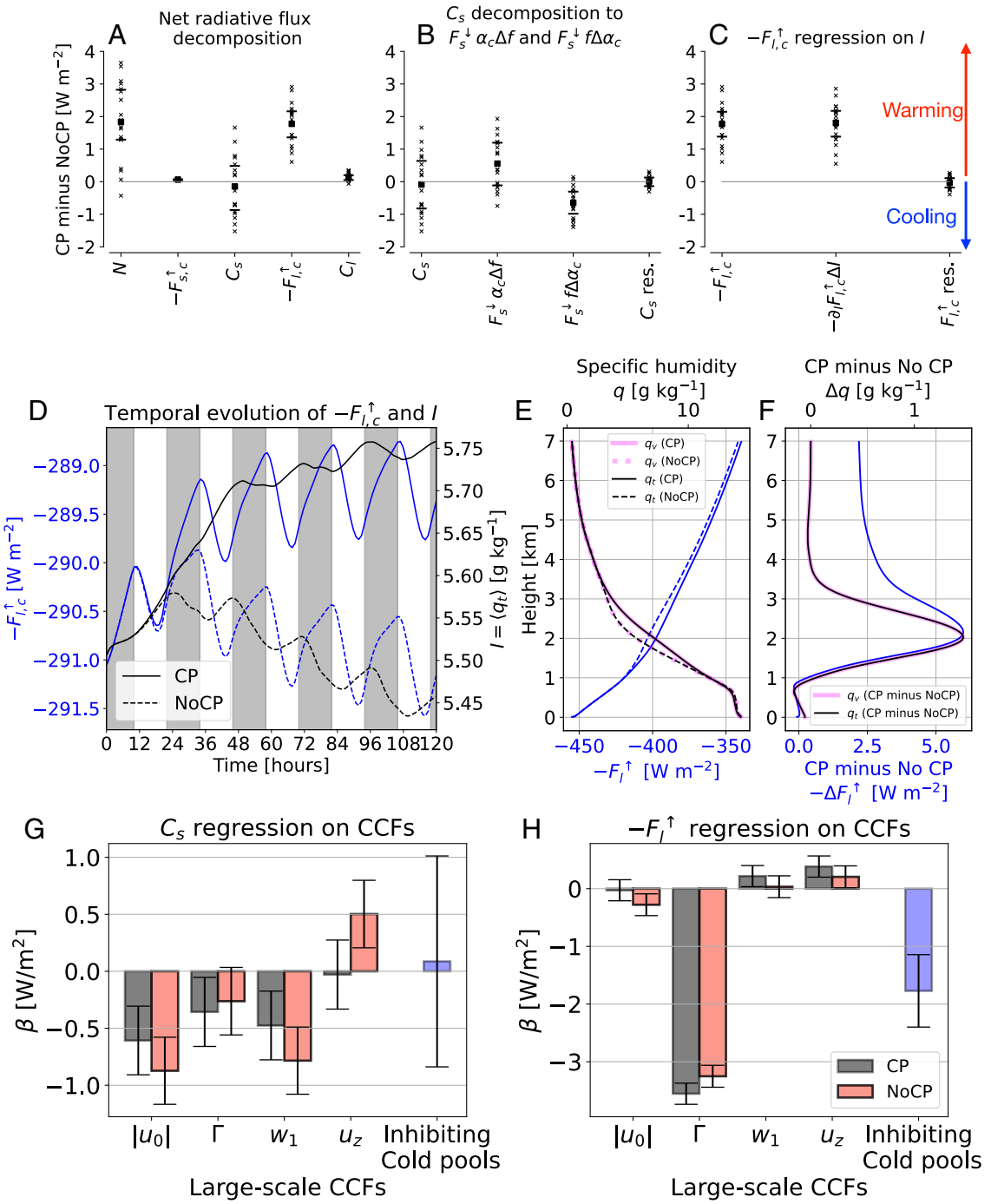

Fig. 2. Effects of cold pools on the daily mean net radiative budget at the top of the atmosphere. (*A*) Decomposition of the net radiative flux at the TOA into shortwave C_s and longwave C_l cloud-radiative effects, and the shortwave $F_{s,c}^{\uparrow}$ and longwave $F_{l,c}^{\uparrow}$ outgoing clear-sky fluxes at the TOA. For each component, the y-axis shows the associated TOA radiation of CP ensemble minus that of NoCP ensemble. All fluxes are averaged over the last (fifth) day of each ensembles' member. Ensemble member means are shown as crosses (×), ensemble means as squares, interquartile ranges as horizontal bars. (*B*) Decomposition of C_s to effects from cloud fraction $F_s^{\downarrow}\alpha_c\Delta f$ and albedo $F_s^{\downarrow} f\Delta\alpha_c$. (*C*) Dependence of $\Delta F_{l,c}^{\uparrow}$ on the difference between the mean total-water path ΔI between the CP and NoCP ensembles. (*D*) Temporal evolution of $-\Delta F_{l,c}^{\uparrow}$ (blue) and I (black) averaged across the entire CP (solid) and NoCP (dashed) ensembles. (*E*) Vertical profiles of upward longwave radiative flux $-F_l^{\uparrow}$ (blue) and total-water specific humidity q_t (black), and water-vapor specific humidity (q_v) averaged over the last (fifth) day and across the entire CP (solid) and NoCP (dashed) ensembles, with their difference (CP minus NoCP) shown in (*F*). (*G* and *H*) Beta (β) coefficients (sensitivities) of the multiple regression of C_s ($R^2 = 0.74$ for the CP and $R^2 = 0.88$ for the NoCP ensemble) and $-F_{l,c}^{\uparrow}$ ($R^2 = 0.99$ for both CP and NoCP ensembles) on CCFs [Note: The larger w_1, the weaker the large-scale subsidence in the ensemble (59)]. The *P*-values of the F-statistic of the model are smaller than 10^{-12}. The impact of inhibiting cold-pool formation (NoCP−CP) is compared with the impact of the unit of change in CCFs.

stability Γ has a larger impact on $-F_{l,c}^{\uparrow}$ than cold pools. The much weaker, uncertain impact of cold pools compared to CCFs on C_s is shown for reference (Fig. 2*G*). The 1.88 W/m^2 of biased cooling at the TOA in the current climate has the potential to influence the longwave clear-sky feedback, given recent findings that emphasize the importance of the contemporary mean state of tropical marine low clouds in shaping their response to warming (63).

At a glance, this result is peculiar. Mesoscale rain evaporation cools the subcloud layer within the cold pools it forms, and dries these regions through diverging downdrafts (35, 40, 44, 45, 61, 64, see also *SI Appendix*, Figs. S4 and S8). Our CP ensemble, too, shows strong drops in temperature and moisture within cold-pool interiors in the subcloud layer (*SI Appendix*, Fig. S8), while the NoCP ensemble does not (*SI Appendix*, Fig. S9). Still, the CP simulations have net warming, while their horizontally averaged, subcloud layer q_t remains unaffected relative to the NoCP simulations (Fig. 2 *E* and *F*). Yet, this is also consistent with observations: The cold-pool fronts are anomalously moist (*SI Appendix*, Fig. S8), indicating that cold pools primarily redistribute moisture horizontally within the subcloud layer. To explain why they still end up with moister cloud layers that warm the trades, we next turn to the moisture budget.

Cold Pools Lead to Lower Drying Rates Due to Weaker Precipitation. To understand why CP simulations' cloud layers remain moister than their NoCP counterparts, we evaluate the "bulk" (vertically integrated) moisture budget in our simulations' lower atmospheres (*Materials and Methods*). The budget is formulated for q_t (cloud water q_l + water vapor q_v, excluding rain water q_r), so it contains sinks of rain production through autoconversion and accretion, and a rain evaporation source. Since this net rain production almost instantaneously leads to its sedimentation (*SI Appendix*, Fig. S1*E*), we call their sum the precipitation flux. Reductions in the CP ensemble's drying from this precipitation flux explain almost their entire relative moistening (Fig. 3*A*). In turn, the smaller precipitation fluxes in the CP ensemble are due to lower rates of rain production by accretion (Fig. 3*B*). In our LES's microphysics scheme, accretion rates are proportional to the product of cloud- and rain-water content, q_l and q_r (65), so we next investigate their differences between the CP and NoCP ensembles.

For rain formation, clouds must deepen. In regimes of shallow cumuli, cloud deepening is correlated with horizontal widening (24, 66). This scale growth is driven by shallow, self-reinforcing mesoscale circulations driven by condensational heating over anomalously moist regions (31–33). We therefore analyze how q_l and q_r relate to the spatial variability in column-integrated total moisture, I', in both ensembles. To this end, we divide the CP and NoCP ensembles into 10-km mesoscale blocks and compute the block-averaged I, denoted I_m. The mesoscale moisture anomaly is then defined as $I' = I_m - \overline{I}$, where $\overline{I}$ is the domain-mean I. Blocks are grouped into bins of ascending I', and for each bin, we compute the average q_l, q_r, and the total-water content anomaly (q_t').

These "moisture-space" plots illustrate that q_t' is consistently positive at all heights where $I' > 0$, and negative where $I' < 0$ (Fig. 3 *C* and *D*). The mesoscale moisture anomalies are concentrated in the upper cloud layers, where they can significantly influence raindrop growth. Indeed, blocks with higher I' host deeper clouds with greater q_l and q_r on top of the elevated q_t anomalies (Fig. 3 *E* and *F*), which in turn drive larger accretion rates and thus more efficient rain production. However, the CP ensemble lacks the extremely moist mesoscale regions with $2 < I' < 3$ g/kg that are present in the NoCP ensemble. It is the presence of these very moist blocks in the NoCP cases which explain their higher ensemble-mean rain production (measured in vertically integrated rain water $\mathcal{R}$, Fig. 3*G*) and surface precipitation flux ($\mathcal{P}$, Fig. 3*H*). That is, the domain-averaged upper cloud layers of the CP ensemble are moister than those of the NoCP ensemble, because the CP ensemble's cloud layers do not have extremely moist mesoscale regions in which condensation and subsequent rain production and sedimentation efficiently depletes the upper cloud layer of water vapor.

By Reducing Mesoscale Ascents, Cold Pools Arrest Mesoscale Self-Aggregation of Moisture. To understand why the CP ensemble lacks extremely moist mesoscale blocks, we perform another moisture budget analysis, but now on the 10-km blocks (*Materials and Methods*). In the CP ensemble, these blocks moisten at a rate 0.31 g/kg/day smaller than in the NoCP ensemble (Fig. 4*A*). This difference is mainly driven by weaker mesoscale circulations (more specific definition in *Materials and Methods*) in the CP ensemble (Fig. 4*A*), which in turn is controlled by a relative weakening of mesoscale vertical ascents w_m' (*SI Appendix*, Fig. S2). The absence of very moist blocks in the CP ensemble is therefore primarily due to their weaker w_m' compared to the NoCP ensemble (Fig. 4*B*). Specifically, since the moistening and drying cycles of these blocks are similar in the CP and NoCP ensembles (*SI Appendix*, Fig. S6), the very moist blocks in the NoCP ensemble arise not because its convective systems live longer, but because they grow to a more vigorous intensity.

To determine how cold pools reduce mesoscale ascent in the CP ensemble, we decompose w_m' into contributions from three regions: inside cold pools, cold-pool edges, and outside cold pools (*SI Appendix*, Fig. S3). We find that cold-pool interiors and edges exert opposing effects: Strong downdrafts within cold-pool interiors, which cover larger areas, are offset by strong updrafts at cold-pool edges, which occupy much smaller fractions (Fig. 4 *D*–*K*). Note that due to the structure of cold-pool-cloud coupling, part of the updrafts are sheared back over cold-pool interiors (44), resulting in some updrafts occurring within cold pools at the cloud level (Fig. 4 *F* and *J*; see also *SI Appendix*, Fig. S4). As a result of the offsetting between the cold-pool interiors and edges, the overall mesoscale ascent in the CP ensemble is governed by regions outside cold pools. On average, w_m' outside cold pools in the CP ensemble evolves similarly to w_m' in the NoCP ensemble (Fig. 4 *B*, *C*, *G*, and *K*). However, because cold pools, when averaged over time and space, occupy ≈20% of these blocks and contribute nearly zero net w_m' (Fig. 4*H*), the overall w_m' in the CP ensemble is reduced relative to the NoCP ensemble.

Summary and Discussion

In summary, the mesoscale patterns in rain evaporation that form cold pools weaken mesoscale vertical ascent and thereby reduce moisture aggregation into very moist mesoscale regions. This reduction prevents the formation of strongly precipitating systems, and their discharge of moisture from the cloud layer. Hence, LESs with cold pools retain moister cloud layers than LESs without them, limiting the emission of longwave clear-sky radiation to space, and leading to a net warming. In our LES ensemble, the average radiative warming from homogenizing rain evaporation (1.88 W/m^2) is comparable to that induced by varying large-scale CCFs over a climatologically representative range.

These findings imply that mesoscale processes have the potential to influence the simulated mean cooling of regimes covered by shallow cumulus clouds, depending on how models treat the interplay between rain evaporation–driven mesoscale descent and moisture aggregation–driven mesoscale ascent, and their effects on large-scale averaged warm rainfall. Traditional GCMs do not

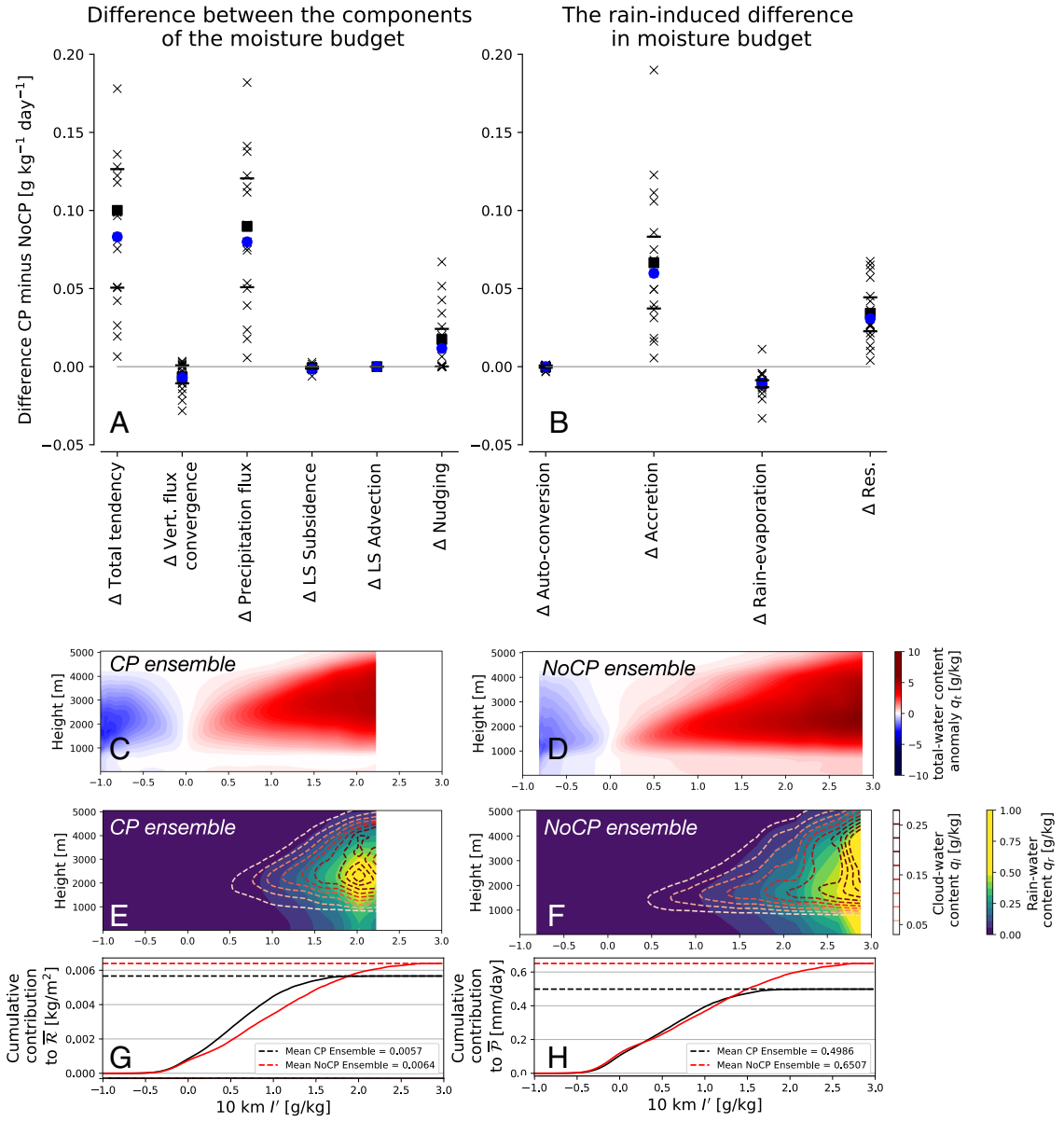

Fig. 3. The impact of cold pools on the bulk moisture budget through precipitation flux. Decomposition of (*A*) the bulk moisture budget and (*B*) the rain-induced difference in moisture budget across ensemble, averaged over hours 12 to 36 when simulations begin diverging in total moisture. Ensemble member means are shown as crosses (×), ensemble means as squares, interquartile ranges as horizontal bars, and the central reference simulation as a blue circle (see *SI Appendix*, Fig. S1 *A–D* for its temporal evolution). (*C–F*) Moisture space of total-water content anomaly q_t', cloud q_l, and rain q_r water contents for CP and NoCP ensembles; q_l is indicated by dashed white-to-red contours. (*G* and *H*) Cumulative contributions of l' bins to ensemble-mean rain-water path $\mathcal{R}$ and surface precipitation flux $\mathcal{P}$ for CP (black) and NoCP (red) ensembles.

represent either mesoscale circulation and would thus require other unresolved scales models (parameterizations) to produce the precipitation drying that in either of our model configurations is driven by the circulations. Conversely, emerging kilometer-scale GCMs (67, 68), which are capable of representing mesoscale self-aggregation (69), likely lack the resolution to resolve shallow cold pools (70), and may thus require parameterizations that represent their effects to not develop a cold bias. Even the LES models used here retain large uncertainties in the representation of turbulence and rain evaporation, which is crudely represented even at resolutions as fine as 100 m. Cold pools have been shown to be sensitive to microphysical parameterizations (71, 72) and LES grid spacing (70). To assess the sensitivity of our results to these factors, we performed two analyses using the central reference simulation with and without cold pools: one with a finer 50 m grid spacing and another with a simpler, single-moment, microphysics scheme (73, 74) compared to the double-moment scheme used in our ensemble (65). Both tests indicate that the impact of homogenizing rain evaporation on total moisture and TOA outgoing longwave radiation remains consistent and significantly dominates the effects of changing horizontal resolution from 100 m to 50 m (*SI Appendix*, Fig. S10) or the choice of microphysics scheme (*SI Appendix*, Fig. S11).

The mesoscale blocks analyzed in this study (≈10 km) are much smaller than the ≈200 km mesoscale circles used in recent observations (48). However, recent research (34) shows that mesoscale vertical motion variability decreases systematically with increasing block size across the 10 km to 700 km range,

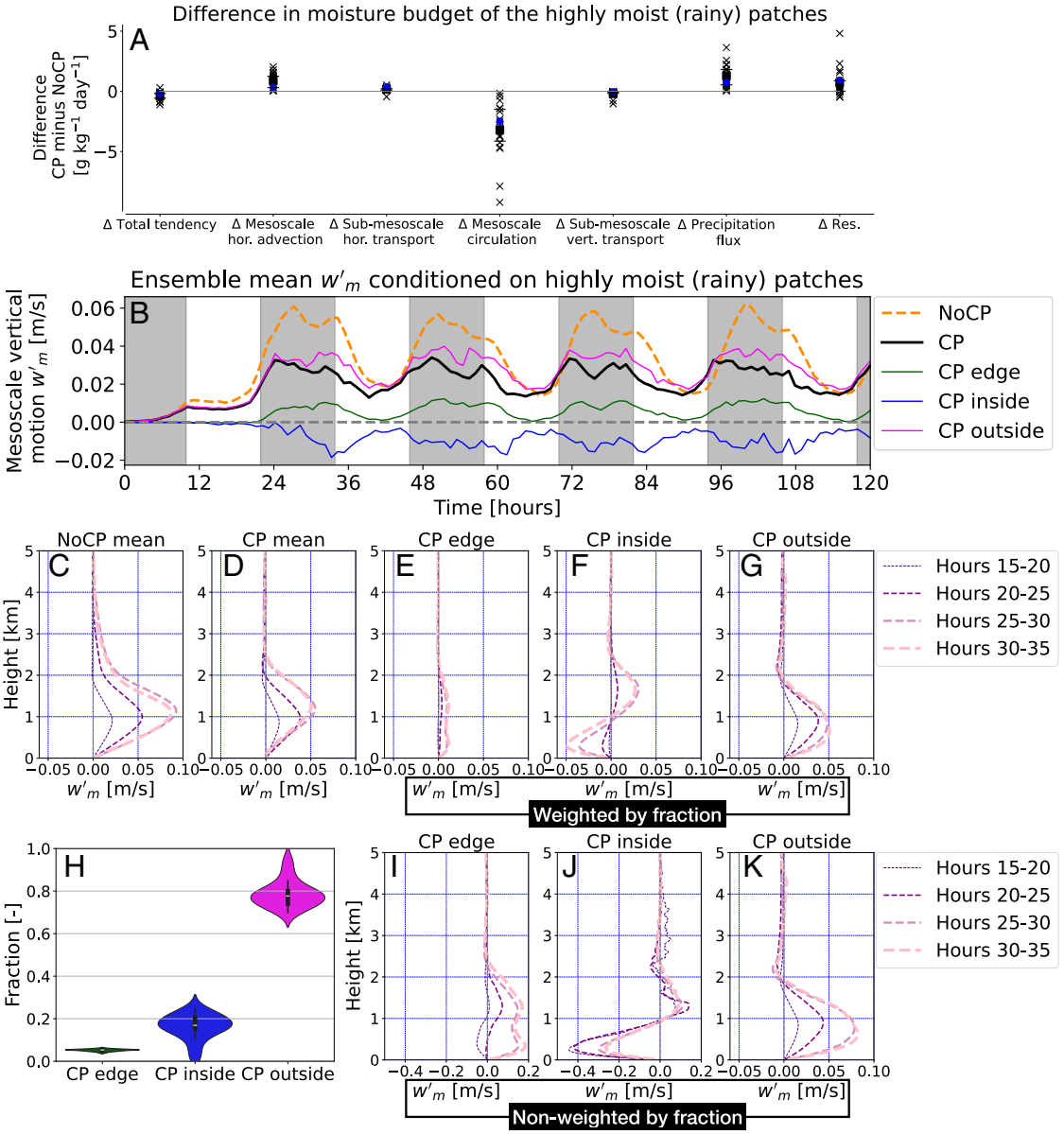

Fig. 4. Impact of cold pools on mesoscale self-aggregation of moisture. (*A*) Differences between terms in Eq. **9** for the CP and NoCP ensembles (see its time series in *SI Appendix*, Fig. S6). At each time step, components are averaged over 10-km blocks where I' exceeds the 90th percentile. Time averages are taken over hours 12 to 36, when the simulations begin to diverge in total moisture. Crosses (×) indicate individual simulation means, squares show the ensemble mean, horizontal bars mark the interquartile range and the central reference simulation as a blue circle. (*B*) Ensemble-averaged time series of mesoscale 10-km vertical motion (w'_m) in the lowest 2 km for NoCP (orange) and CP (black), with CP contributions from cold-pool edges (green), inside (blue), and outside (magenta). (*C*–*G*) Vertical profiles of (*B*) for hours 15 to 35. (*H*) The distribution of the fractions of cold-pool regions within highly moist (rainy) 10-km blocks. (*I*-*K*) Same as (*E*-*G*) but without weighting by fractions of cold-pool regions in (*H*). Similar figures for panels (*C*–*K*) for the last day of the ensemble is shown by *SI Appendix*, Fig. S7.

with the latter often taken as the upper bound of mesoscale dynamics. Thus, our 10 km block size lies at the lower end of this mesoscale spectrum and is therefore representative for the mesoscale. At the same time, the total LES domain size (≈150 km) is too small to capture the very large (>700 km) mesoscale patterns that arise from extratropical disturbances intruding into the trade-wind region. Therefore, how cold pools influence such larger-scale structures and their associated radiative balance at the TOA remains an open question for future research.

Despite the presence of stratiform anvils in our LES ensemble (44, 59), the ensemble-mean cloud cover (0.12) remains much smaller than reported values from recent field campaign observations (0.42) (75). Future work should investigate the sensitivity of these missing optically thin clouds to cold pools and whether they could meaningfully affect the results shown in Fig. 2*B*.

Our results also depend on the selected method of process denial. Had we removed or weakened rain evaporation directly, rather than homogenized it (e.g., refs. 76 and 77) we would directly have altered the domain-mean cooling and drying rates (41, 50), and their impact on TOA radiation. Our results, instead, show that even if one correctly predicts the average rain evaporation on the scale of a GCM grid box, its natural mesoscale variability within such a domain adds a significant, internal feedback to the mean state.

We therefore stress that the main result of our study is not the precise value of the CP-induced TOA warming averaged over our subset of environments, simulation configurations, and method of process-denial. Rather, our main result is the identification of a pathway through which significant warming can occur by mesoscale processes; we now require more detailed analyses of its robustness in other process models, and of the realism of its links in observations.

Notably, the mesoscale cloud processes affect the mean cooling not through the clouds themselves, but through their organization of clear-sky water vapor. This is consistent with recent observational examinations of the subtropics (62), but also with analyses of the tropical deep convective regime, which show that: i) cold pools suppress convective self-aggregation (28, 50, 78), and ii) self-aggregation leads to mean drying of the tropics and enhances longwave clear-sky radiative cooling (29). Therefore, we are now finding mechanisms across both tropical and subtropical regimes, through which mesoscale organization can shape clear-sky, longwave radiation. Hence, future work should explore whether adding shallow mesoscale circulations to our theoretical frameworks, observational analyses, and global numerical models alters their estimated clear-sky longwave feedback.

Materials and Methods

Ensembles of Large-Eddy Simulations. To assess the impact of cold pools on top-of-atmosphere radiative budgets, we performed two 19-member ensembles of large-domain ($153.6 \times 153.6\,km^2$) large-eddy simulations (LESs), with 100 m horizontal and 20 m vertical resolution. Both ensembles are subsets of the *Cloud Botany* ensemble (59), which is forced by climatologically relevant large-scale cloud-controlling factors (CCFs) of the trade-wind regime, deduced from ERA5 reanalysis data (58). In this study, we select only those CCFs to which cold pools are sensitive (Table 1). Previous studies on the full ensemble (44, 45) show that cold pools are strongly modulated by the geostrophic wind speed $|u_0|$ and subsidence w_1, and to a lesser extent by free-tropospheric stability Γ and wind shear u_z. As each CCF increases from weak to strong, cold-pool number and size increase from nearly zero to larger values, making this subset representative of the full ensemble.

We could have added a fifth dimension of variability-one to which cold pools are relatively insensitive, such as free-tropospheric humidity-to our subset. In that case, this fifth CCF would need to be varied while keeping the other four CCFs (which strongly control cold pools) fixed at their values in the central reference simulation. As a result, cold-pool characteristics would remain similar across all simulations in that dimension. Consequently, the impact of homogenizing rain evaporation on the radiative budgets would match that of the central reference simulation, which is close to the ensemble mean (Figs. 3 *A* and *B* and 4*A*). Therefore, including a fifth CCF to which cold pools are insensitive would not alter our estimates of the radiative impact of suppressing cold-pool formation across the ensemble.

Calculation of Cloud Fraction and Albedo. Cloud fraction f_c is a standard output of the *Cloud Botany* ensemble and is computed as the ratio of cloudy grid cells (those with cloud-water path greater than zero) to the total number of grid cells in the simulation domain. The domain-mean cloud albedo α_c is calculated as the ratio of the domain-mean shortwave cloud-radiative effect C_s to the product of the domain-mean incoming shortwave radiation and cloud fraction, $F_s^{\downarrow} \times f_c$. The shortwave cloud-radiative effect C_s is obtained as the difference between all-sky and clear-sky shortwave radiative fluxes at the TOA. Both radiative fluxes, as well as the incoming shortwave radiation, are standard outputs of the *Cloud Botany* ensemble.

Moisture Budget Analysis for the Full Domain. We analyze moisture budget for the mass-weighted vertical average of total-water specific humidity q_t, defined as

$$I = \langle q_t \rangle = \frac{\int_0^{z_\infty} \rho(z) q_t(z) dz}{\int_0^{z_\infty} \rho(z) dz}, \quad [1]$$

where $\rho(z)$ denotes the reference density profile, and z_∞ is the domain top at 7 km. The variation of term I is primarily driven by the boundary layer (extending from the surface to the top of the trade-wind inversion layer) processes across the ensemble (*SI Appendix*, Fig. S5). Applying the mass-weighted averaging operator, defined as

$$\langle \circ \rangle = \frac{\int_0^{z_\infty} \rho(z) \circ dz}{\int_0^{z_\infty} \rho(z) dz}, \quad [2]$$

to all terms in the moisture budget equation, we obtain the bulk moisture budget:

$$\frac{\partial I}{\partial t} = \underbrace{\frac{\partial \langle q_t \rangle}{\partial t}}_{\text{Bulk moisture tendency}} = - \underbrace{\left\langle \frac{\partial \left(\overline{w' q_t'} \right)}{\partial z} \right\rangle}_{\text{Vertical flux convergence}} - \underbrace{\left\langle u_j^{LS} \left(\frac{\partial q_t}{\partial x_j} \right)^{LS} \right\rangle}_{\text{Large-scale advection and subsidence}} - \underbrace{\langle P(z) \rangle}_{\text{Precipitation}} + \underbrace{\langle N \rangle}_{\text{Nudging}}, \quad [3]$$

where u_j^{LS} represents the large-scale velocity in the j-direction, $\overline{w' q_t'}$ is the slab-mean total moisture flux at height z with

$$X' = X - \overline{X}, X \in \{w, q_t\}, \quad [4]$$

where X' is anomaly of variable X with respect to the slab-mean average $\overline{X}$. $P(z)$ is the domain-mean total precipitation flux at height z. Specifically, $P(z)$ is the sum of autoconversion, accretion, and rain evaporation fluxes. Note that the moisture profile in each member of the *Cloud Botany* ensemble is nudged toward its initial horizontally averaged value with the nudging term in Eq. **3** (59).

Moisture Budget Analysis for the Mesoscale Blocks. Similar analysis of Eq. **3** can be written for the 10-km, mesoscale blocks; however, the mesoscale blocks also experience horizontal moisture fluxes at their boundaries with adjacent

Table 1. Parameters of the LES ensemble

Large-scale and initial conditions	Parameters [units]	No. of simulations	Range of variability
Near-surface geostrophic wind speed	u_0 [m/s]	5	From 5 to 15
Temperature lapse rate in the free troposphere	Γ [K/km]	5	From 4.5 to 7.5
Large-scale vertical velocity variability	w_1 [cm/s]	4	From −0.002 to 0.001
Shear in the horizontal geostrophic wind	u_z [(m/s)/km]	4	From −4 to 4

Overall information about the ensemble's parameters determining CCFs. Note that in addition to simulations above, the ensemble has a central reference simulation with the mean of CCFs above. This means our ensemble features 19 simulations in total.

mesoscale blocks. Thus, the mesoscale blocks' moisture budget can be expressed as

$$\frac{DI}{Dt} = \frac{D\langle q_t\rangle}{Dt} = \underbrace{-\left\langle \frac{\partial (U'_{h_j} q_t)}{\partial x_j} \right\rangle}_{\text{i}} \underbrace{-\left\langle \frac{\partial (w' q_t)}{\partial z} \right\rangle}_{\text{ii}} - \underbrace{\left\langle u_j^{LS} \left(\frac{\partial q_t}{\partial x_j} \right)^{LS} \right\rangle}_{\text{Large-scale advection and subsidence}} - \underbrace{\langle P(z) \rangle}_{\text{Precipitation}} + \underbrace{\langle N \rangle}_{\text{Nudging}}, \quad [5]$$

where the first (i) and second (ii) terms on the right-hand side represent the total q_t flux in the horizontal and vertical, respectively. Here, U'_{h_j} and w' denote the horizontal and vertical components of the anomalous velocity vector with respect to the domain mean. This means that the horizontal advection with the domain-mean horizontal wind is absorbed in the left-hand side of Eq. **5**, which means our budget analysis follows the mesoscale blocks as they move with the larger-scale wind.

To understand the contributions from the mesoscales and submesoscales, we decompose variables $\phi \in \{U'_{h_j}, w'\}$ to contributions from the mesoscales ϕ_m and submesoscales ϕ_s. The mesoscale contributions ϕ_m are calculated by averaging ϕ over each 10-km block. For each 100-m grid cell inside a 10-km block, submesoscale contributions ϕ_s is anything that remains after filtering the mesoscale contributions, i.e. $\phi_s = \phi - \phi_m$. By applying the product rule to the first two terms (i and ii) of Eq. **5**, we obtain

$$\langle \text{i}_m \rangle = -\left\langle U'_{h_{j,m}} \frac{\partial q_{t,m}}{\partial x_j} \right\rangle - \left\langle q_{t,m} \frac{\partial U'_{h_{j,m}}}{\partial x_j} \right\rangle - \left\langle \frac{\partial (U'_{h_{j,s}} q_{t,s})_m}{\partial x_j} \right\rangle, \quad [6]$$

$$\langle \text{ii}_m \rangle = -\left\langle w'_m \frac{\partial q_{t,m}}{\partial z} \right\rangle - \left\langle q_{t,m} \frac{\partial w'_m}{\partial z} \right\rangle - \left\langle \frac{\partial (w'_s q'_{t,s})_m}{\partial z} \right\rangle. \quad [7]$$

The mass conservation at the mesoscales implies that $q_{t,m} \frac{\partial U'_{h_{j,m}}}{\partial x_j} + q_{t,m} \frac{\partial w'_m}{\partial z} = 0$. Substituting this relation, we obtain

$$\langle \text{i}_m \rangle + \langle \text{ii}_m \rangle = \underbrace{-\left\langle U'_{h_{j,m}} \frac{\partial q_{t,m}}{\partial x_j} \right\rangle}_{\text{mesoscale horizontal advection}} \underbrace{-\left\langle \frac{\partial (U'_{h_{j,s}} q_{t,s})_m}{\partial x_j} \right\rangle}_{\text{submesoscale horizontal transport}} \underbrace{-\left\langle w'_m \frac{\partial q_{t,m}}{\partial z} \right\rangle}_{\text{gradient production}} \underbrace{-\left\langle \frac{\partial (w'_s q'_{t,s})_m}{\partial z} \right\rangle}_{\text{submesoscale vertical transport}}. \quad [8]$$

In Fig. 4*A*, we refer to the term "gradient production" as "mesoscale circulation" to make it more accessible to a general reader. Because the 10-km blocks in both ensembles experience the same external large-scale subsidence and advection and are similarly nudged toward their initial state, we include both terms in the residual and rewrite Eq. **5** as

$$\frac{DI_m}{Dt} = \frac{D\langle q_{t,m}\rangle}{Dt} = \langle \text{i}_m \rangle + \langle \text{ii}_m \rangle - \langle P_m(z) \rangle + \text{Residual}_m. \quad [9]$$

To analyze moisture aggregation in the very moist blocks of both ensembles, we calculate the terms of Eq. **9** for these blocks at each hour for each ensemble member. At every time step, the terms are averaged over blocks where mesoscale moisture anomaly I'_m exceeds the 90th percentile of its distribution for that time step. This condition closely resembles averaging over blocks where the rain-water path exceeds the 90th percentile of its distribution. The differences in the terms of Eq. **9** between the CP and NoCP ensembles are shown in Fig. 4*A*. This comparison helps identify which term is responsible for the higher humidity in the very moist blocks of the NoCP ensemble compared to their counterparts in the CP ensemble.

Data, Materials, and Software Availability. Original data created for this study, including atmospheric simulation outputs and the Python scripts to reproduce figure results, are available in a persistent repository (Zenodo) at https://doi.org/10.5281/zenodo.15544026 (79). In addition, the version of the Dutch Atmospheric Large-Eddy Simulation used for homogenizing rain evaporation is publicly available at Github https://github.com/dalesteam/dales/tree/botany-homogenization.

ACKNOWLEDGMENTS. P.A. deeply thanks Steven Boing for his help on homogenizing rain evaporation in the Dutch Atmospheric Large-Eddy Simulation. During the time working on this research, P.A. received support from The Branco Weiss Fellowship–Society in Science, administered by ETH Zurich. This publication is part of the Veni project Connecting the Clouds with file number VI.Veni.242.017, financed by the Dutch Research Council (NWO) under the grant [grant ID https://doi.org/10.61686/TJSFP13491]. P.A. and M.J. acknowledge support from the International Space Science Institute (ISSI) in Bern, through ISSI International Team project 576 ("Constraining Trade-Cumuli Feedback by Means of Process Understanding"). This research used computational resources of Fugaku provided by RIKEN through the High-Performance Computing Infrastructure (HPCI) System Research Project (Project ID: hp240116). We also acknowledge Cooperating University Computing Facilities (Samenwerkende Universitaire Rekenfaciliteiten SURF-www.surf.nl) for making the National Supercomputer Snellius accessible for running and analyzing the sensitivity experiments to the grid spacing and choice of microphysics scheme. Finally, we thank the two anonymous reviewers for their constructive and helpful feedback which improved the quality of this study.

Author affiliations: [a]Department of Geoscience and Remote Sensing, Delft University of Technology, Delft 2628 CN, The Netherlands; and [b]Department of Meteorology and Air Quality, Wageningen University and Research, Wageningen 6700 AA, The Netherlands

Author contributions: P.A. and M.J. designed research; P.A. and M.J. performed research; P.A., M.J., and F.J. contributed new reagents/analytic tools; P.A. analyzed data; P.A. data visualization; performing LES; pre- and postprocessing of data; F.J. providing feedback for review and editing; compiling the Large-Eddy Simulation models with homogenized rain evaporation; securing grants for the supercomputer Fugaku; and P.A. and M.J. wrote the paper.

1. S. Bony, J. L. Dufresne, H. Le Treut, J. J. Morcrette, C. Senior, On dynamic and thermodynamic components of cloud changes. *Clim. Dyn.* **22**, 71–86 (2004).
2. S. Bony, J. L. Dufresne, Marine boundary layer clouds at the heart of tropical cloud feedback uncertainties in climate models. *Geophys. Res. Lett.* **32**, L20806 (2005).
3. J. Vial, J. L. Dufresne, S. Bony, On the interpretation of inter-model spread in CMIP5 climate sensitivity estimates. *Clim. Dyn.* **41**, 3339–3362 (2013).
4. S. Bony *et al*., Clouds, circulation and climate sensitivity. *Nat. Geosci.* **8**, 261–268 (2015).
5. T. Schneider *et al*., Climate goals and computing the future of clouds. *Nat. Clim. Chang.* **7**, 3–5 (2017).
6. L. Nuijens, A. P. Siebesma, Boundary layer clouds and convection over subtropical oceans in our current and in a warmer climate. *Curr. Clim. Chang. Rep.* **5**, 80–94 (2019).
7. M. D. Zelinka *et al*., Causes of higher climate sensitivity in CMIP6 models. *Geophys. Res. Lett.* **47**, e2019GL085782 (2020).
8. S. C. Sherwood *et al*., An assessment of Earth's climate sensitivity using multiple lines of evidence. *Rev. Geophys.* **58**, e2019RG000678 (2020).
9. P. N. Blossey *et al*., Marine low cloud sensitivity to an idealized climate change: The CGILS LES intercomparison. *J. Adv. Model. Earth Syst.* **5**, 234–258 (2013).
10. J. Radtke, T. Mauritsen, C. Hohenegger, Shallow cumulus cloud feedback in large eddy simulations-bridging the gap to storm resolving models. *Atmos. Chem. Phys. Discuss.* **2020**, 1–19 (2020).
11. G. V. Cesana, A. D. Del Genio, Observational constraint on cloud feedbacks suggests moderate climate sensitivity. *Nat. Clim. Chang.* **11**, 213–218 (2021).

12. T. A. Myers *et al*., Observational constraints on low cloud feedback reduce uncertainty of climate sensitivity. *Nat. Clim. Chang.* **11**, 501–507 (2021).
13. R. Vogel *et al*., Strong cloud-circulation coupling explains weak trade cumulus feedback. *Nature* **612**, 696–700 (2022).
14. J. Vial, A. L. Albright, R. Vogel, I. Musat, S. Bony, Cloud transition across the daily cycle illuminates model responses of trade cumuli to warming. *Proc. Natl. Acad. Sci. U.S.A.* **120**, e2209805120 (2023).
15. N. Bellouin *et al*., Bounding global aerosol radiative forcing of climate change. *Rev. Geophys.* **58**, e2019RG000660 (2020).
16. P. Stier *et al*., Multifaceted aerosol effects on precipitation. *Nat. Geosci.* **17**, 719–732 (2024).
17. B. Stevens *et al*., Sugar, gravel, fish and flowers: Mesoscale cloud patterns in the trade winds. *Q. J. R. Meteorol. Soc.* **146**, 141–152 (2020).
18. M. Janssens *et al*., Cloud patterns in the trades have four interpretable dimensions. *Geophys. Res. Lett.* **48**, e2020GL091001 (2021).
19. L. Denby, Discovering the importance of mesoscale cloud organization through unsupervised classification. *Geophys. Res. Lett.* **47**, e2019GL085190 (2020).
20. S. Rasp, H. Schulz, S. Bony, B. Stevens, Combining crowdsourcing and deep learning to explore the mesoscale organization of shallow convection. *Bull. Am. Meteorol. Soc.* **101**, E1980–E1995 (2020).
21. S. Bony, H. Schulz, J. Vial, B. Stevens, Sugar, gravel, fish, and flowers: Dependence of mesoscale patterns of trade-wind clouds on environmental conditions. *Geophys. Res. Lett.* **47**, e2019GL085988 (2020).
22. H. Schulz, R. Eastman, B. Stevens, Characterization and evolution of organized shallow convection in the downstream north Atlantic trades. *J. Geophys. Res. Atmos.* **126**, e2021JD034575 (2021).
23. H. Schulz, C^3ONTEXT: a common consensus on convective organization during the EUREC^{4}A experiment. *Earth Syst. Sci. Data* **14**, 1233–1256 (2022).
24. P. Alinaghi *et al*., Shallow cumulus cloud fields are optically thicker when they are more clustered. *Q. J. R. Meteorol. Soc.* **150**, 3566–3577 (2024).
25. L. Denby, Charting the realms of mesoscale cloud organisation using unsupervised learning. arXiv [Preprint] (2023). http://arxiv.org/abs/2309.08567 (Accessed 15 November 2025).
26. I. Tobin, S. Bony, R. Roca, Observational evidence for relationships between the degree of aggregation of deep convection, water vapor, surface fluxes, and radiation. *J. Clim.* **25**, 6885–6904 (2012).
27. C. J. Muller, I. M. Held, Detailed investigation of the self-aggregation of convection in cloud-resolving simulations. *J. Atmos. Sci.* **69**, 2551–2565 (2012).
28. C. Muller, S. Bony, What favors convective aggregation and why? *Geophys. Res. Lett.* **42**, 5626–5634 (2015).
29. S. Bony *et al*., Observed modulation of the tropical radiation budget by deep convective organization and lower-tropospheric stability. *AGU Adv.* **1**, e2019AV000155 (2020).
30. T. Heus *et al*., Formulation of the Dutch atmospheric large-eddy simulation (dales) and overview of its applications. *Geosci. Model. Dev.* **3**, 415–444 (2010).
31. C. S. Bretherton, P. Blossey, Understanding mesoscale aggregation of shallow cumulus convection using large-eddy simulation. *J. Adv. Model. Earth Syst.* **9**, 2798–2821 (2017).
32. P. Narenpitak, J. Kazil, T. Yamaguchi, P. Quinn, G. Feingold, From sugar to flowers: A transition of shallow cumulus organization during ATOMIC. *J. Adv. Model. Earth Syst.* **13**, e2021MS002619 (2021).
33. M. Janssens *et al*., Nonprecipitating shallow cumulus convection is intrinsically unstable to length scale growth. *J. Atmos. Sci.* **80**, 849–870 (2023).
34. M. Janssens, G. George, H. Schulz, F. Couvreux, D. Bouniol, Shallow convective heating in weak temperature gradient balance explains mesoscale vertical motions in the trades. *J. Geophys. Res. Atmos.* **129**, e2024JD041417 (2024).
35. P. Zuidema *et al*., On trade wind cumulus cold pools. *J. Atmos. Sci.* **69**, 258–280 (2012).
36. A. Seifert, T. Heus, Large-eddy simulation of organized precipitating trade wind cumulus clouds. *Atmos. Chem. Phys.* **13**, 5631–5645 (2013).
37. Z. Li, P. Zuidema, P. Zhu, Simulated convective invigoration processes at trade wind cumulus cold pool boundaries. *J. Atmos. Sci.* **71**, 2823–2841 (2014).
38. R. Vogel, L. Nuijens, B. Stevens, The role of precipitation and spatial organization in the response of trade-wind clouds to warming. *J. Adv. Model. Earth Syst.* **8**, 843–862 (2016).
39. P. Zuidema, G. Torri, C. Muller, A. Chandra, A survey of precipitation-induced atmospheric cold pools over oceans and their interactions with the larger-scale environment. *Surv. Geophys.* **38**, 1283–1305 (2017).
40. R. Vogel, H. Konow, H. Schulz, P. Zuidema, A climatology of trade-wind cumulus cold pools and their link to mesoscale cloud organization. *Atmos. Chem. Phys.* **21**, 16609–16630 (2021).
41. K. C. Helfer, L. Nuijens, The morphology of simulated trade-wind convection and cold pools under wind shear. *J. Geophys. Res. Atmos.* **126**, e2021JD035148 (2021).
42. O. Lamaakel, G. Matheou, Organization development in precipitating shallow cumulus convection: Evolution of turbulence characteristics. *J. Atmos. Sci.* **79**, 2419–2433 (2022).
43. O. Lamaakel, R. Venters, J. Teixeira, G. Matheou, Computational domain size effects on large-eddy simulations of precipitating shallow cumulus convection. *Atmosphere* **14**, 1186 (2023).
44. P. Alinaghi, A. P. Siebesma, F. Jansson, M. Janssens, F. Glassmeier, External drivers and mesoscale self-organization of shallow cold pools in the trade-wind regime. *J. Adv. Model. Earth Syst.* **17**, e2024MS004540 (2025).
45. P. Alinaghi, F. Jansson, D. A. Blázquez, F. Glassmeier, Cold pools mediate mesoscale adjustments of trade-cumulus fields to changes in cloud droplet number concentration. *Atmos. Chem. Phys.* **25**, 6121–6139 (2025).
46. S. Bony *et al*., EUREC4A: A field campaign to elucidate the couplings between clouds, convection and circulation. *Surv. Geophys.* **38**, 1529–1568 (2017).
47. B. Stevens *et al*., EUREC4A. *Earth Syst. Sci. Data Discuss.* **2021**, 1–78 (2021).
48. G. George, B. Stevens, S. Bony, R. Vogel, A. K. Naumann, Widespread shallow mesoscale circulations observed in the trades. *Nat. Geosci.* **16**, 584–589 (2023).
49. M. Janssens, F. Jansson, P. Alinaghi, F. Glassmeier, A. P. Siebesma, Symmetry in mesoscale circulations explains weak impact of trade cumulus self-organization on the radiation budget in large-eddy simulations. *Geophys. Res. Lett.* **52**, e2024GL112288 (2025).
50. S. J. Böing, H. J. Jonker, A. P. Siebesma, W. W. Grabowski, Influence of the subcloud layer on the development of a deep convective ensemble. *J. Atmos. Sci.* **69**, 2682–2698 (2012).
51. B. Stevens, J. Brenguier, "Cloud controlling factors: Low clouds" in *Clouds in the Perturbed Climate System*, J. Heintzenberg, R. Charlson, Eds. (MIT Press, 2009).
52. Klein, S. A., Hall, A., Norris, J. R., Pincus, R. (2017). Low-Cloud Feedbacks from Cloud-Controlling Factors: A Review. In: Pincus, R., Winker, D., Bony, S., Stevens, B. (eds) Shallow Clouds, Water Vapor, Circulation, and Climate Sensitivity. Space Sciences Series of ISSI, vol **65**. Springer, *Cham*. https://doi.org/10.1007/978-3-319-77273-8_7.
53. T. A. Myers, J. R. Norris, Observational evidence that enhanced subsidence reduces subtropical marine boundary layer cloudiness. *J. Clim.* **26**, 7507–7524 (2013).
54. R. C. Scott *et al*., Observed sensitivity of low-cloud radiative effects to meteorological perturbations over the global oceans. *J. Clim.* **33**, 7717–7734 (2020).
55. J. C. Golaz, V. E. Larson, W. R. Cotton, A pdf-based model for boundary layer clouds. Part I: Method and model description. *J. Atmos. Sci.* **59**, 3540–3551 (2002).
56. F. Hourdin *et al*., Unified parameterization of convective boundary layer transport and clouds with the thermal plume model. *J. Adv. Model. Earth Syst.* **11**, 2910–2933 (2019).
57. D. Walters *et al*., The met office unified model global atmosphere 7.0/7.1 and Jules global land 7.0 configurations. *Geosci. Model. Dev.* **12**, 1909–1963 (2019).
58. H. Hersbach *et al*., The ERA5 global reanalysis. *Q. J. R. Meteorol. Soc.* **146**, 1999–2049 (2020).
59. F. Jansson *et al*., Cloud Botany: Shallow cumulus clouds in an ensemble of idealized large-domain large-eddy simulations of the trades. *J. Adv. Model. Earth Syst.* **15**, e2023MS003796 (2023).
60. N. Rochetin, C. Hohenegger, L. Touzé-Peiffer, N. Villefranque, A physically based definition of convectively generated density currents: Detection and characterization in convection-permitting simulations. *J. Adv. Model. Earth Syst.* **13**, e2020MS002402 (2021).
61. L. Touzé-Peiffer, R. Vogel, N. Rochetin, Cold pools observed during EUREC4A: Detection and characterization from atmospheric soundings. *J. Appl. Meteorol. Climatol.* **61**, 593–610 (2022).
62. B. Fildier, C. Muller, R. Pincus, S. Fueglistaler, How moisture shapes low-level radiative cooling in subsidence regimes. *AGU Adv.* **4**, e2023AV000880 (2023).
63. P. Ceppi, T. Myers, P. Nowack, C. Wall, M. Zelinka, Implications of a pervasive climate model bias for low-cloud feedback. *Geophys. Res. Lett.* **51**, e2024GL110525 (2024).
64. S. P. de Szoeke, E. D. Skyllingstad, P. Zuidema, A. S. Chandra, Cold pools and their influence on the tropical marine boundary layer. *J. Atmos. Sci.* **74**, 1149–1168 (2017).
65. A. Seifert, K. D. Beheng, A double-moment parameterization for simulating autoconversion, accretion and selfcollection. *Atmos. Res.* **59**, 265–281 (2001).
66. G. Feingold *et al*., Analysis of albedo versus cloud fraction relationships in liquid water clouds using heuristic models and large eddy simulation. *J. Geophys. Res. Atmos.* **122**, 7086–7102 (2017).
67. B. Stevens *et al*., DYAMOND: The dynamics of the atmospheric general circulation modeled on non-hydrostatic domains. *Prog. Earth Planet. Sci.* **6**, 1–17 (2019).
68. M. Satoh *et al*., Global cloud-resolving models. *Curr. Clim. Chang. Rep.* **5**, 172–184 (2019).
69. L. Saffin *et al*., Kilometer-scale simulations of trade-wind cumulus capture processes of mesoscale organization. *J. Adv. Model. Earth Syst.* **15**, e2022MS003295 (2023).
70. R. Fiévet, B. Meyer, J. O. Haerter, On the sensitivity of convective cold pools to mesh resolution. *J. Adv. Model. Earth Syst.* **15**, e2022MS003382 (2023).
71. Z. Li, P. Zuidema, P. Zhu, H. Morrison, The sensitivity of simulated shallow cumulus convection and cold pools to microphysics. *J. Atmos. Sci.* **72**, 3340–3355 (2015).
72. J. Kazil *et al*., "Cold Pool Analysis from The Cold Pool Model Intercomparison Project (CP-MIP)" in 105th Annual AMS Meeting 2025 (American Meteorological Society Meeting Abstracts, 2025), vol. **105**, 448635. https://ui.adsabs.harvard.edu/abs/2025AMS...10548635K/abstract.
73. W. W. Grabowski, Toward cloud resolving modeling of large-scale tropical circulations: A simple cloud microphysics parameterization. *J. Atmos. Sci.* **55**, 3283–3298 (1998).
74. H. Tomita, New microphysical schemes with five and six categories by diagnostic generation of cloud ice. *J. Meteorol. Soc. Jpn.* **86A**, 121–142 (2008).
75. T. Mieslinger *et al*., Optically thin clouds in the trades. *Atmos. Chem. Phys. Discuss.* **2021**, 1–33 (2021).
76. S. B. Nissen, J. O. Haerter, Circling in on convective self-aggregation. *J. Geophys. Res. Atmos.* **126**, e2021JD035331 (2021).
77. Y. L. Hwong, C. J. Muller, The unreasonable efficiency of total rain evaporation removal in triggering convective self-aggregation. *Geophys. Res. Lett.* **51**, e2023GL106523 (2024).
78. N. Jeevanjee, D. M. Romps, Convective self-aggregation, cold pools, and domain size. *Geophys. Res. Lett.* **40**, 994–998 (2013).
79. P. Alinaghi, M. Janssens, F. Jansson, Dataset for the cold-pool denial experiment in a large ensemble of large-domain, high-resolution large-eddy simulations [Data set]. *Zenodo*. https://doi.org/10.5281/zenodo.17215561. Deposited 27 September 2025.